Astron. Astrophys. 298, 894–904 (1995)

ASTRONOMY
AND
ASTROPHYSICS

A submillimetre continuum study of S 140/L 1204: the detection of three new submillimetre sources and a self-consistent model for the region

Nigel R. Minchin[1], **Derek Ward-Thompson**[2], **and Glenn J. White**[1]

[1] Department of Physics, Queen Mary and Westfield College, University of London, Mile End Road, London E1 3NS, UK
[2] Royal Observatory, Blackford Hill, Edinburgh EH9 3HJ, UK

Received 16 September 1994 / Accepted 15 November 1994

Abstract. We present submillimetre continuum observations of the L 1204/S 140 complex in broad bands centred at 450, 800 and 1100μm. The morphology of the region is similar at all three wavelengths, with the emitting region compact, about 90 arcsec in diameter, and centrally peaked around the cloud core. Three new submillimetre continuum sources are observed which are not coincident with any previously known near or mid-infrared sources. We designate the sources S 140-SMM1–3. SMM1 is roughly coincident with a previously known NH_3 clump and 2.7mm source, and near-IR reflection nebulosity from the surface of SMM2 has previously been seen. The three submillimetre continuum sources may be protostellar in nature, although it is not possible to determine whether they are gravitationally bound, since virial mass estimates are disrupted by the presence of an energetic bipolar outflow. For this reason, earlier claims that the 2.7mm source in SMM1 is collapsing appear somewhat premature. The observation that SMM1 and SMM2 lie either side of the infrared sources, in a line roughly perpendicular to the direction of the bipolar outflow, imply they may be the remnants of a large-scale disk.

Comparison of the continuum emission with previous high resolution CS, NH_3 and CI observations provides evidence that, for the first time, demonstrates the photon-dominated region and outflow are intimately linked. The only scenario that is able to explain all of the available molecular and atomic emission line data and our submillimetre continuum data, is one in which the outflow has expanded towards the edge of the molecular cloud and the edge of the blueshifted outflow lobe is now bounded by the expanding HII region. The NH_3 and continuum emission emanate from the inner edge of the outflow lobe, shielded from the external UV field.

A plot of the 800μm flux against N($C^{18}O$) implies that the dust/gas mass ratio is close to the canonical value (~1%) at the lower end of the observed extinction range ($A_v \leq 70$), but for the highest observed extinctions (A_v =70–100) the continuum flux density increases rapidly, implying a higher dust/gas mass ratio is appropriate (~2-5%), possibly indicating freeze-out of gas onto dust grains.

Key words: stars: early-type – interstellar medium: HII regions – jets and outflows

Send offprint requests to: Nigel R. Minchin

1. Introduction

The L 1204 molecular cloud/S 140 HII region complex is one of the most fascinating and complex regions for observing the interaction of an embedded molecular outflow and a photon-dominated region (PDR) with their parent molecular cloud.

At the southwestern extremity of the L 1204 molecular cloud is an edge-illuminated PDR (e.g. Blair et al. 1978; Evans et al. 1987; White & Padman 1991), adjacent to the S 140 HII region, powered by the nearby B0 star HD 211880. The complex lies at a distance of 910 pc (Crampton & Fisher 1974). Only ~70 arcsec to the northeast of the PDR is an embedded cluster of three infrared sources (e.g. Beichman et al. 1979) which lie at the centre of a high-velocity molecular outflow (e.g. Bally & Lada 1983; Snell et al. 1984), and which have been identified as three embedded stars of spectral type B1.5–B2 (Evans et al. 1989). The outflow axis is along the southeast-northwest direction, parallel to the PDR. The blue and redshifted outflow lobes are separated by ~35 arcsec, with a high degree of overlap, implying the outflow axis is directed close to the line of sight.

Minchin et al. (1993–hereafter Paper I) recently compared high-resolution (~10 arcsec), single velocity channel, [CI] $^3P_1 \rightarrow {}^3P_0$ observations of White & Padman (1991) to various ^{12}CO and ^{13}CO emission line maps. The CI emission is mainly confined to a clumpy, elongated, ridge-like feature adjacent to the edge of the molecular cloud and coincident with a similar feature seen in ^{12}CO emission. The coincidence of the CI and CO features is interpreted as evidence that the molecular material is highly clumpy. This allows the UV radiation to penetrate

into the cloud before dissociating carbon-bearing molecules, producing CI at the clump edges. There is a second region of intense CI emission, extending to the northeast *away from* the PDR, towards the centre of the cloud. This is contradictory to PDR models, and has led to speculation that it is produced by the radiation field from the embedded infrared cluster (Hayashi & Murata 1992; Paper I).

Recent multi-channel observations of the [CI] $^3P_1$–$^3P_0$ line (also at ~10 arcsec) not only confirm that CI emission emanates from the PDR adjacent to the HII region/molecular cloud interface, but also reveals intense CI emission towards the outflow source, mainly at velocities blue and redshifted relative to the ambient cloud, not covered by the White & Padman observations (Minchin et al. 1994 – hereafter Paper II). There is also an arc of blue and redshifted emission extending from the peak for at least 30 arcsec to the south, which is adjacent to a similar feature observed in blueshifted $C^{17}O$ J=3→2 emission. This implies the CI emission originates from the inner edge of the blueshifted molecular outflow wall. It is argued that the most plausible mechanism for producing the CI emission from the outflow region is the effect of shocks on the physical and chemical processes at the interface between the stellar wind and the blueshifted outflow cavity wall. A more extensive $C^{18}O$ J=3→2 emission line map confirms the arc feature observed in CI and $C^{17}O$ J=3→2 emission, but also reveals a second, similar arc feature extending towards the east (Minchin et al. 1994–hereafter Paper III). It is thus an example of the classic 'tuning fork' morphology, where emission at the ambient cloud velocity is tracing the outflow cavity wall of the blueshifted lobe.

In this paper we present the first submillimetre continuum maps of the L 1204/S 140 region. The outline of the paper is as follows: Sect. 2 outlines the observational details; the new observations are presented in Sect. 3; physical properties of the emitting dust are discussed in Sect. 4.1; in Sect. 4.2 we compare the 800μm emission map with recent high resolution molecular and atomic line maps and discuss implications for the morphology of the region; in Sect. 4.3 we examine possible variations in the dust/gas mass ratio across the region; Sect. 5 lists the main conclusions of the paper.

2. Observations

The observations were carried out at the James Clerk Maxwell Telescope[1] (JCMT), located on Mauna Kea, Hawaii. The 450, 800 and 1100 μm observations were all obtained on the mornings of 1993 April 20 to 24, 01:30–09:30 HST (UT = 11:30–19:30). The detector used was the common-user receiver UKT14, which contains a single-element, ^{3}He-cooled Ge:In:Sb bolometer, and a series of filters matched to the atmospheric transmission windows (Duncan et al. 1990). The observations were carried out while using the secondary mirror to chop in azimuth at around 7 Hz and synchronously to detect the signal, thus rejecting 'sky' emission. Photometry was carried out using a chop throw of 60 arcsec and a FWHM beam-size of 18 arcsec throughout, while maps were made using chop throws of 30, 40 and 60 arcsec and diffraction-limited FWHM beam-sizes of 8, 13 and 18 arcsec at 450, 800 and 1100μm respectively.

Calibration was performed using the planet Uranus (Orton et al. 1986; Griffin & Orton 1993) as the primary calibrator, and the bright submillimetre continuum source G34.3 (Sandell 1994) as a secondary calibrator, which were measured in all wavebands at least once per hour, to measure the detector sensitivity at each waveband. Throughout the observations, estimates were obtained of the atmospheric opacity at each waveband, based on the monitoring of the opacity at 225 GHz provided by the NRAO radiometer, located at the Caltech Submillimetre Observatory (CSO), using standard ratios. This continuous monitoring of calibration sources of known intensity, together with the 225 GHz opacity, allowed the atmospheric opacity, τ, to be calculated at all times, in all wavebands, and a fully consistent calibration was obtained.

All maps were made in dual-beam 'on-the-fly' raster mode, where the telescope is scanned in azimuth and elevation, while simultaneously chopping in azimuth. Beam maps were made of Uranus, and maps were made of G34.3, to calibrate the maps of S 140, and to estimate the effect of the error-beam of the telescope at the shorter wavelengths on extended source flux measurements. A total of 6, 4 and 3 maps, each of 1 second per point, were made of S 140 at 450, 800 and 1100μm, sampling every 3, 4 and 5 arcsec respectively, ensuring that all maps were over-sampled.

Altogether, we estimate our total absolute calibration uncertainty to be ~20 per cent at 800 and 1100μm, and ~30 per cent at 450μm. The 450μm atmospheric transmission at zenith varied through the run from 5 to 40% on different nights. The highest frequency observations were carried out during the periods of maximum transmission. Pointing and focus checks were performed typically once per hour. The focus was found to be very stable throughout, and the pointing was observed to be accurate to better than 3 arcsec.

3. Results

Figs 1a–c show isophotal contour maps of the S 140 region at 450, 800 and 1100μm respectively. The origin of the maps is RA (1950) = $22^h\ 17^m\ 42^s$, Dec. (1950) = +63° 03′ 45″, the position of peak CO emission for the molecular cloud (Paper I). The submillimetre continuum emission traces the cold dust in the molecular cloud and should delineate the extent of the cold cloud core. It can be seen that the morphology of the three maps looks very similar. There is a region of strong submillimetre emission about 90 arcsec in diameter, centred around the three embedded infrared sources (e.g. Hackwell et al. 1982). This emission is bounded sharply to the west and southwest, in the direction of the edge-on PDR, while in the other directions the emission falls off more gradually. The total flux densities on the maps, measured in a 90×90 arcsec square aperture are: 754 Jy at 450μm, 106 Jy at 800μm and 55 Jy at 1100μm.

[1] The James Clerk Maxwell Telescope is operated by the Royal Observatories, on behalf of the UK PPARC, the Netherlands Organisation for Pure Research, and the National Research Council of Canada.

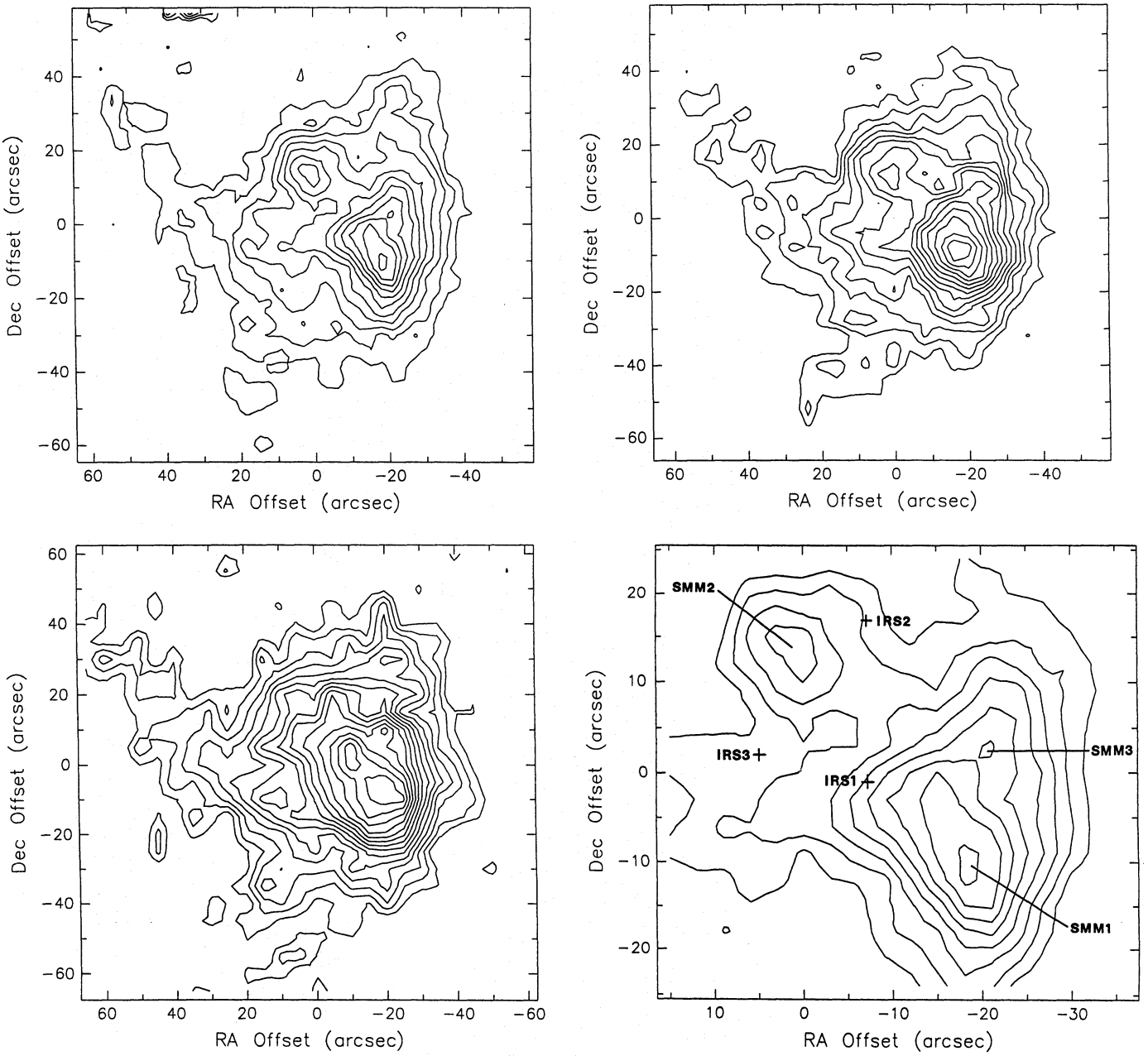

Fig. 1a–d. Isophotal contour maps of the submillimetre continuum emission from S 140. **a** 450μm map. The base level contour is 5 Jy/beam (2σ) and the contour interval is 2.5 Jy/beam. **b** 800μm map. The base level contour is 1.5 Jy/beam (4σ) and the contour interval is 0.5 Jy/beam. **c** 1100μm map. The base level contour is 0.75 Jy/beam (3σ) and the contour interval is 0.25 Jy/beam. **d** 450μm map for the central 50×50 arcsec^2. The positions of the three submillimetre sources, S 140-SMM1–3 are marked, as are the positions of the three infrared sources, IRS1–3

The peak of the submillimetre continuum emission is offset from the origin of the maps, and lies at roughly (-17, -10), and we here designate this brightest submillimetre peak S 140-SMM1. Note that this is not coincident with the CO, CI or CO isotope peaks (Papers I, II and III). A ridge of emission extends northwards from SMM1 for approximately 50 arcsec, and there is a low-level diffuse arm of emission extending over an arcminute to the northeast. This ridge and diffuse arm have a roughly horseshoe-shaped morphology, similar to that observed in CS and NH_3 emission, to which we will return in Sect. 4.2. There is a secondary peak to the northeast of SMM1 at an offset of (0, +14), which we here designate S 140-SMM2.

Figure 1d shows a close-up of the central region of the 450μm isophotal contour map to outline the key features more clearly. SMM1 and 2 are marked, and in addition, a third, subsidiary peak can be seen at approximate coordinates (-23, +5), which we here name S 140-SMM3. This peak is not so clear or well-defined as the other two sources, and lies on the edge of the extended SMM1 peak. Also marked on Fig. 1d are the three 10 and 20μm sources, IRS1-3, of Hackwell et al. (1982). It can be

Table 1. Flux densities of the three submillimetre continuum peaks of S 140 quoted to 2 sig. figs. For each source at each wavelength three different estimates of the flux density are provided: the peak flux density per diffraction-limited beam (8 arcsec at 450μm, 13 arcsec at 800μm and 18 arcsec at 1100μm); the extended flux density measured in a square aperture of given dimensions; and a gaussian fit to each source, after an estimated background level has been subtracted (the FWHM of the fitted gaussians are also listed). The calibration errors are $\pm$30% at 450μm and $\pm$20% at 800 and 1100μm. However, there are additional uncertainties in the gaussian flux densities due to contamination from the extended cloud emission and due to source confusion – it was not possible to measure the extended flux density of SMM3, because of confusion with SMM1

Source Name	R.A. (1950)	Dec. (1950)	λ (μm)	Peak flux (Jy) (diff.lim.beam)	Extended flux (Jy)	Box size (arcsec)	Gaussian flux (Jy)	FWHM (arcsec)
S 140-SMM1	$22^h\ 17^m\ 39.5^s$	+63° 03′ 35″	450	33	90	21×21	45	12×20
			800	8.5	15	20×20	8.2	14×21
			1100	4.2	6.3	25×25	4.3	18×25
S 140-SMM2	$22^h\ 17^m\ 42.0^s$	+63° 03′ 59″	450	24	60	21×21	14	9×9
			800	5.3	9.8	20×20	3.2	14×14
			1100	3.2	5.2	25×25	1.8	18×18
S 140-SMM3	$22^h\ 17^m\ 38.6^s$	+63° 03′ 50″	450	27	–	–	9.3	9×9
			800	5.8	–	–	2.6	13×13
			1100	3.6	–	–	1.5	18×18

seen that none of the new submillimetre sources is coincident with any of the infrared sources.

Table 1 lists the flux densities of the three sources S 140-SMM1–3 estimated in three different ways: the peak flux density per diffraction-limited beam; the extended flux density measured in a square aperture; and a gaussian fit to each source, after an estimated background level has been subtracted. There are uncertainties in each of these methods because it is difficult to distinguish between the emission from each source and the extended emission due to the S 140 cloud. This was the reason for attempting to fit the sources with gaussians, to try to discriminate between extended emission and source emission.

The peak and extended flux densities of the three sources appear somewhat similar, with SMM1 being the brightest, likewise the gaussian-fitted flux densities of SMM1 are the largest. The gaussians were fitted by subtracting off an extended component, due to the diffuse cloud emission, and then fitting a gaussian to each of the remaining peaks. This is somewhat subjective and we estimate the absolute uncertainties in the gaussian flux densities could be as high as 50%. The gaussian flux densities of SMM3 probably contain the largest uncertainties, due to confusion with SMM1.

The source FWHM listed in the final column of Table 1 are the best guide to the source sizes. SMM1 appears to have a FWHM of roughly 18 arcsec north-south, and to be unresolved east-west at 800 and 1100μm. However, it is marginally resolved east-west at 450μm, yielding a deconvolved FWHM of 9 arcsec. SMM2 and 3 are basically point sources. The above observations yield the conclusions that the three submillimetre sources are real sources, which are not scale-free, but have definite sizes which are listed in Table 2.

The nature of the sources is less certain. As mentioned above, they do not coincide with any previously known infrared sources. However, the observation that SMM1 and SMM2 lie either side of the infrared sources, in a line roughly perpendicular to the direction of the bipolar outflow, may indicate that they are related. One possible explanation could be that the sources SMM1 and 2 are the remnants of some kind of disk which was originally collimating the outflow, but has subsequently broken up to form discrete sources. This is similar to the case of S106, as observed by Richer et al. (1993).

4. Discussion

4.1. Physical properties of the submillimetre sources

The S 140 region is associated with the IRAS PSC (Beichman et al. 1988) point source IRAS22176+6303. This source is coincident with the submillimetre emission we have mapped here, and has quoted flux densities of: 308.35 Jy at 12μm, 1540.32 Jy at 25μm, 11232 Jy at 60μm and 13463 Jy at 100μm. These flux densities sample emission from the entire region we have mapped, due to the lower resolution of the IRAS survey, hence we can compare them with the submillimetre flux densities for the whole region, which we quote in Sect. 3 above.

Figure 2a shows the spectral energy distribution of the whole cloud in the infrared and submillimetre regimes. The solid line is a grey-body curve of the form:

$$S(\nu) = \Omega B(\nu, T)(1 - e^{-\tau}) \quad (1)$$

where Ω is the solid angle of the emitter, B(ν, T) is the blackbody function, the optical depth $\tau = (\nu/\nu_c)^\beta$, ν_c is the critical

Table 2. Source parameters of the three submillimetre continuum peaks of S 140: S 140-SMM1, S 140-SMM2 & S 140-SMM3

Source Name	FWHM (arcsec)	FWHM (pc)	Temperature (K)	Mass ($M_\odot$)	Density $\times 10^6 cm^{-3}$	Luminosity ($L_\odot$)
S 140-SMM1	9×18	0.04×0.08	35^{+15}_{-20}	$16.6^{+40}_{-5.9}$	3.0–16	940–1370
S 140-SMM2	9×9	0.04×0.04	35^{+15}_{-20}	$6.5^{+16}_{-2.3}$	3.9–21	330–570
S 140-SMM3	9×9	0.04×0.04	35^{+15}_{-20}	$5.3^{+13}_{-1.9}$	3.2–17	≤230

frequency at which the optical depth is 1, and β is the dust grain opacity. The grey-body curve shown has T=35K and β=1.5, and is consistent with the longer wavelength data, under the assumption that the submillimetre emission is optically thin. This value of β has been shown to give values for molecular cloud masses derived from the submillimetre continuum dust emission, which are consistent with those derived from other methods, such as optically thin molecular line tracers, in dense cloud regions (e.g. André et al. 1993). The highest temperature consistent with the data longward of 60μm is 50K, although there is excess emission at the shorter 12 and 25μm wavebands indicating additional hotter components of the emitting dust. The lowest temperature consistent with the submillimetre data alone is 15K.

A dust temperature of 35^{+15}_{-20}K is consistent with the excitation temperature of the gas, assumed to be ~50K from low CO line temperatures, suggesting that the dust and gas are probably in equilibrium, although there is probably colder dust in the dense cores SMM1-3. There is also a suggestion that the 1100μm data may be high relative to the 800μm flux density, possibly indicating the presence of free-free emission at the longer wavelength.

The flux densities due to the individual sources, taken from column 8 of Table 1, are shown in Fig. 2b–d, along with grey-body curves all with T=35K and β=1.5, but with different solid angles. Also shown on Figs. 2b and 2c are 10 and 20μm upper limits to SMM1 and 2 estimated from the maps of Hackwell et al. (1982), whose data do not quite extend to SMM3. These upper limits are estimated for a 9×18 arcsec box for SMM1 and a 9×9 arcsec box for SMM2. In addition it can be seen on the 20μm image of Hackwell et al. (1982) that there is a possible source (at no more than a 2σ level) at the position of SMM1. We estimate from the map that this source has a flux density of approximately 3.4 Jy at 20μm. This is marked with a cross on Fig. 2b. This may well be a real detection of this source, since it lies close to our optimum fit to the submillimetre data, requiring only a small increase in temperature above the 35K greybody to account for the flux.

Thus the range of temperatures of the dust emitting in the submillimetre regime is 35^{+15}_{-20}K. This is consistent with the range of temperatures of 40–50K for the sources IRS1–3 observed by Lester et al. (1986). From this we can calculate masses from the submillimetre data. We can derive masses for each of the three submillimetre sources, using the equation relating submillimetre flux density to gas mass, modified from Hildebrand (1983) in the form:

$$M_{\rm gas} = [S(\nu)D^2]/[B(\nu,T)\kappa] \quad (2)$$

where symbols take their usual meanings and κ is the dust mass opacity, which depends on β. Since we have measured β=1.5, and using a dust to gas mass ratio of 100, we obtain a value for κ of 0.016 cm^2g^{-1}, similar to that found by Rengarajan (1984). This is the same value as was used in measurements of the ρ Oph A molecular cloud by André et al. (1993), which yielded a mass calculated from the dust for the whole ρ Oph A ridge which was in good agreement with that estimated from molecular line tracers. From this we calculate the masses of SMM1-3 listed in Table 2. The range of mass values quoted corresponds to the uncertainty in the dust temperature. We can also calculate the mean density within the FWHM of each source using the source sizes measured in the previous section. These are also listed in Table 2. It can be seen that the mean densities of all three sources are approximately the same – ~10^6-10^7 cm^{-3}. The large uncertainty in the masses arises from the uncertainty in the dust temperature, which cannot be further constrained without higher resolution far-infrared data, and from the non-linear behaviour of equation 2 in the low-temperature regime.

The virial masses of the three sources can theoretically be estimated from the velocity dispersion towards each of them. However, all molecular line tracers are broadened by the proximity of the bipolar outflow, even the usual high-density tracing CS lines, thus we can only place upper limits on the virial masses. The approximate velocity dispersion towards each of the sources is taken to be <3kms^{-1} from the CS J=3→2 and J=7→6 line spectra (Stutzki et al. 1994). Therefore the virial masses within the FWHM quoted in Table 2 are <30$M_\odot$, <20$M_\odot$ and <20$M_\odot$ for SMM1, 2 and 3 respectively. Unfortunately this does not allow us to say definitely whether or not the sources are gravitationally bound, until some sufficiently high density tracer is found which is not affected by the outflow.

The long-wavelength luminosity of the entire S 140 cloud region can be estimated by integrating under the data-points of Fig. 2a, from 12 to 1100μm. We calculate this total far infrared

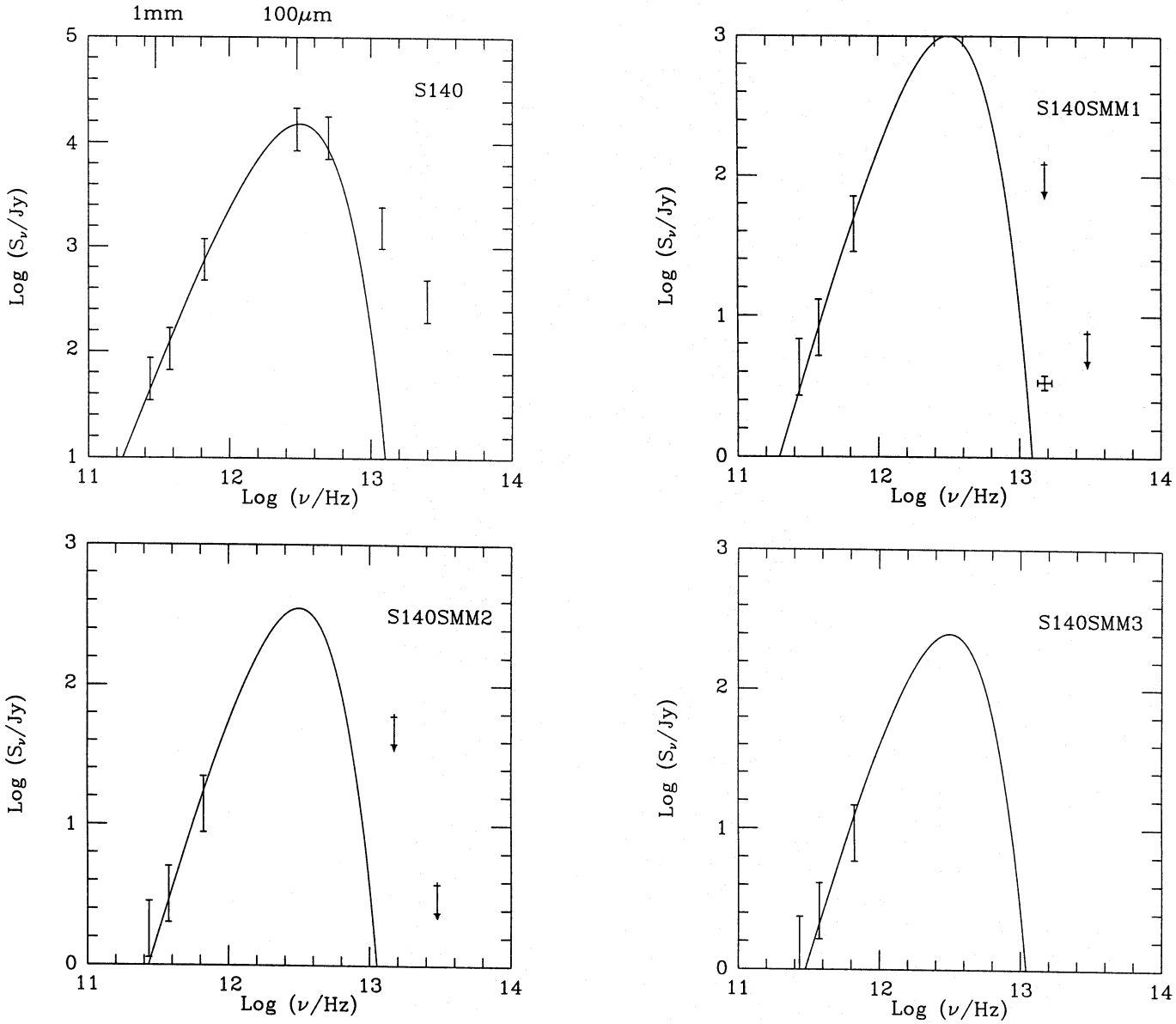

Fig. 2. a Spectral energy distribution (SED) of the whole cloud in the infrared and submillimetre regimes. The submillimetre data are the flux densities measured in a 1.5×1.5 arcmin^2 box, encompassing the whole cloud, and the infrared data are the IRAS PSC flux densities for the source 22176+6303. The solid line is a grey-body consistent with the data, with T = 35K and β=1.5. **b** SED of SMM1, showing a grey-body with the same T and β as in **a**, but with a different solid angle. The 10 and 20μm upper limits are estimated from the maps of Hackwell et al. (1982), and the cross represents a tentative 20μm source detection by Hackwell et al. **c** Same as **b** for SMM2. **(d)** Same as **(b)** for SMM3 (no mid-infrared data exists for this source)

and submm luminosity to be $\sim 2.3\times10^4 L_\odot$. Likewise, from Figs 2b–d we can estimate the 10–1100μm luminosities of SMM1–3, and these are listed in Table 2. The lower limit is integrated under the grey-body curve in each case. The upper limits for SMM1 and 2 are calculated by treating the 10 and 20μm upper limits as if they were detections. These luminosities scale relative to the total far infrared luminosity of the cloud approximately in the ratio of the submillimetre flux densities. The observed luminosity could be a combination of heating internal to the molecular cloud, and external illumination by the adjacent HII region. We cannot say whether there are additional heating sources buried within the submillimetre sources (although we cannot rule that out), without higher resolution and higher sensitivity far-infrared data.

SMM1, the brightest of the three submillimetre continuum peaks, was detected by Zhou et al. (1993) at 2.7mm, although they failed to detect SMM2 or 3. They noted that their continuum detection was coincident with an NH_3 peak, which they call clump 3. Their measured gas temperature towards clump 3 is 45K, consistent with our data, and they derive a velocity dispersion of 3.9kms^{-1} from NH_3, also in approximate agreement with the CS observations. They interpret the observed line pro-

file towards clump 3 as indicating gravitational collapse, based on the observation of a double-peaked NH_3 line profile. Their model predicts a central stellar mass of $10M_\odot$, a kinetic temperature of 45K and a density of $n\sim10^6$ cm^{-3}, all of which are in close agreement with our estimates. Their estimated accretion luminosity ($50L_\odot$) is considerably less than our total estimated luminosity for SMM1 ($<1370L_\odot$). However, their interpretation of the line profile as indicating collapse is somewhat premature, given the confusion caused to line-shapes by the bipolar outflow.

SMM2 contains within its FWHM contour two apparent near-infrared sources observed by Evans et al. (1989) – their source numbers 13 and 14. However, due to the high levels of polarisation of these sources, they were ascribed to clumps of reflection nebulosity by these latter authors. We can now see that they represent reflected illumination from the surface of SMM2. None of the other near-infrared sources coincides with our new submillimetre sources.

4.2. The morphology of the region

4.2.1. Comparison of the continuum observations with recent atomic and molecular line data

Figure 3 shows the contours of 800μm continuum emission overlayed upon greyscale images of the CS J = 1→0 (Hayashi & Murata 1992), NH_3 (1,1) (Zhou et al. 1993) and CI $^3P_1$–$^3P_0$ (White & Padman 1991) line emission.

Before discussing each figure in detail, let us point out some general similarities. Figures 3a–c show there to be a prominent, elongated ridge of emission extending from south of the infrared sources (shown on each of the figures) to the northeast – designated the eastern ridge. There is a second, though less prominent and extensive, ridge extending from the southwest of the infrared sources to the northwest – designated the western ridge. This feature is particularly bright in CS emission, but is also clearly observed in NH_3 and submm continuum emission (at all three of the observed wavelengths), but is not seen in CI emission.

The CS J=1→0 line emission (Fig 3a) is resolved into a clumpy, horseshoe-shaped structure, with a diameter of ~0.3pc, width of ~0.05pc, a total mass of $60M_\odot$, and individual clump masses of 0.3-8.5$M_\odot$ (Hayashi & Murata 1992). The CS map has an effective resolution of 10 arcsec, slightly higher than the 14 arcsec resolution of the 800μm observations. The position of peak continuum emission (SMM1) is offset by ~12 arcsec to the northeast of the main peak of CS emission, designated peak G by Hayashi & Murata, with a derived mass of $8.5M_\odot$ at position RA (1950) = $22^h\ 17^m\ 37^s.78$, Dec. (1950) = +63° 03′ 28″.9. Both the CS and continuum peaks lie along a line directed northeast-southwest that also points towards the external illuminating star, HD211880, and the embedded IR sources. Both the eastern and western CS ridge features appear to be located 10–20 arcsec outside of the more compact and centrally peaked continuum emission.

The NH_3 (1,1) emission (Fig. 3b) also delineates a clumpy horseshoe morphology at the high resolution of the Zhou et al. observations (5 arcsec FWHM). Although the basic morphology is similar to the CS J=1→0 line, the eastern ridge is more elongated (~2.5 arcmin compared to ~1.5 arcmin), but the western ridge is noticeably less prominent and extended. The comparison between continuum and NH_3 (1,1) emission is better than for the CS or CI lines, with both eastern and western ridges closely coincident. The main NH_3 peak, designated clump 3 by Zhou *et al*, is at position RA (1950) = $22^h\ 17^m\ 38^s.9$, Dec. (1950) = +63° 03′ 32″, between the continuum and CS peaks and along the same line that also contains the external illuminating star and embedded infrared sources. The closer positional agreement between the NH_3 and continuum peaks may imply that NH_3 is enhanced by evaporation from heated dust grains, or could simply be due to the fact that CS is more difficult to excite than NH_3.

The CI $^3P_1$–$^3P_0$ line emission (Fig. 3c) is the integrated intensity in a 1.3 km s^{-1} channel centred at -8 km s^{-1} (White & Padman 1991) and thus traces emission at the ambient velocity of the molecular cloud. There is intense CI emission from the eastern ridge which, like the NH_3 emission, is closely coincident with the equivalent continuum emission feature. Conversely, the western ridge is not seen in CI emission. There is, however, a clumpy, elongated ridge-like feature adjacent to the southwestern edge of the molecular cloud. This is the position of the edge-on PDR and has been discussed in detail elsewhere (e.g. Papers I, II and III and references therein). The lack of significant continuum, CS or NH_3 emission from the PDR is in accord with models of both homogeneous and clumpy molecular clouds (e.g. Tielens & Hollenbach 1985; van Dishoeck & Black 1988; Hollenbach et al. 1991; Stutzki et al. 1988).

Full velocity coverage of the CI $^3P_1$–$^3P_0$ line, for a limited part of the outflow/PDR regions, was presented in Paper II. This agrees closely with the White & Padman (1991) single channel image, but does not extend across the region of the eastern ridge. It should be pointed out that there *is* considerable CI emission from positions towards the infrared sources, but this is produced within the outflow and is thus observed at blue and redshifted velocities. Hence it was not observed in the single channel observations of White & Padman.

Clearly the S 140 region is extremely complex, with certain aspects of the observations seemingly contradictory. In particular, how can CI emission from the eastern ridge feature be explained? The observation of CI emission from the PDR at the southwestern edge of the cloud is as expected from clumpy cloud models (Papers I and II), but the presence of an elongated CI feature that is almost orthogonal to the plane of the PDR is puzzling. The fact that the northern extension to the blueshifted CO emission (Paper I) lies even further within the eastern ridge feature may suggest that this is the limb-brightened edge to the northern extension of the blueshifted outflow lobe. As CS is a high density tracer this would seemingly agree with the scenario of a dense swept-up shell of material at the outer edge of an outflow cavity wall.

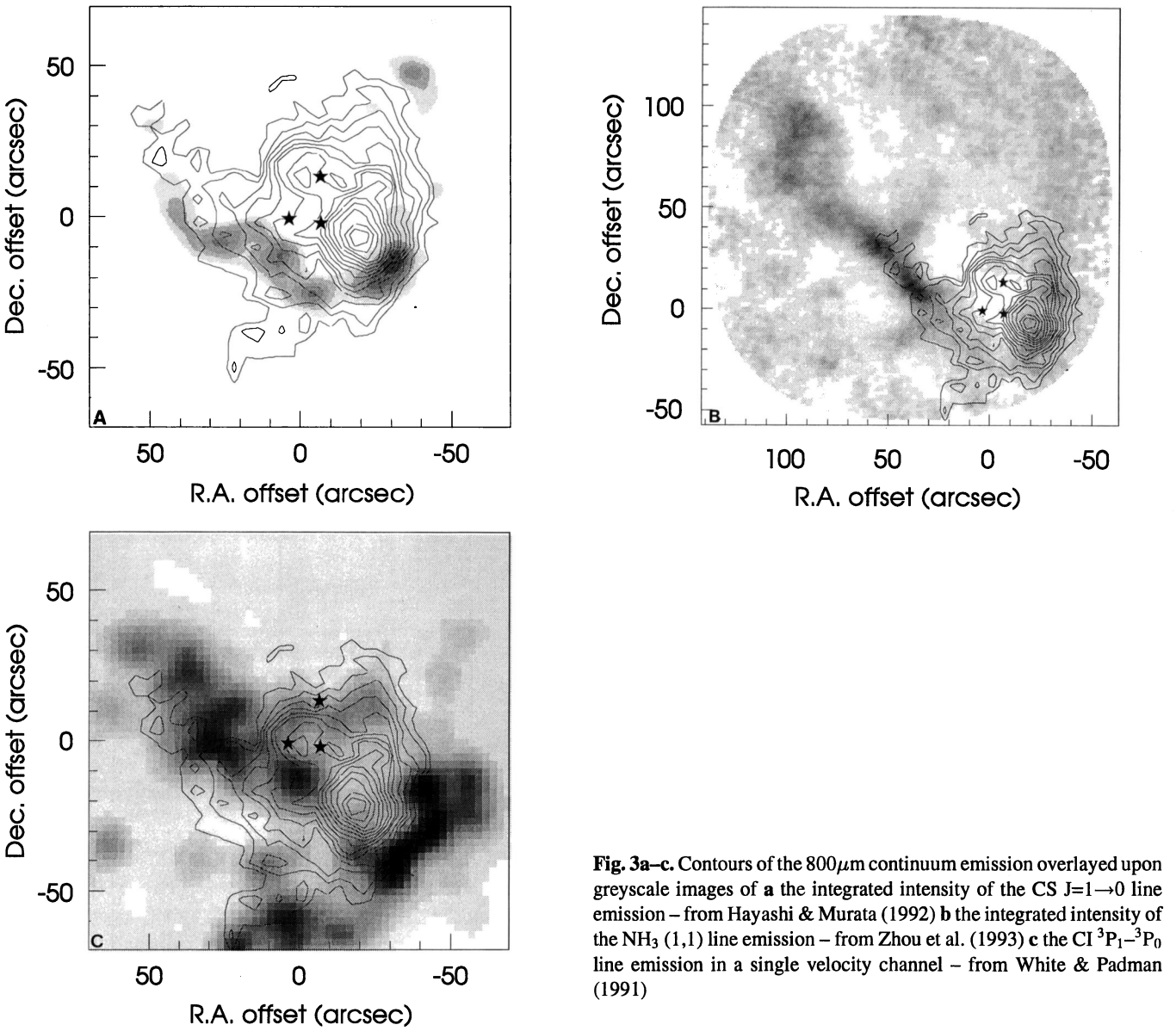

Fig. 3a–c. Contours of the 800μm continuum emission overlayed upon greyscale images of **a** the integrated intensity of the CS J=1→0 line emission – from Hayashi & Murata (1992) **b** the integrated intensity of the NH_3 (1,1) line emission – from Zhou et al. (1993) **c** the CI $^3P_1$–$^3P_0$ line emission in a single velocity channel – from White & Padman (1991)

We also know that the CI emission is coincident with the NH_3 and continuum emission along the eastern ridge, *all* of which are offset from the CS emission. This contradicts PDR models, and is in marked contrast to observations of the PDR at the southwestern edge of the molecular cloud. As discussed in Papers I, II and III, at this position the only significant observed emission is from CI and ^{12}CO (due to effective self-shielding and clumpy structure) lines. Significant CS, NH_3 and submm continuum emission is only observed behind the PDR, at the positions of clump G, clump 3 and SMM1 respectively. The CS emission peak is observed to be *closer* towards the PDR than either the NH_3 or continuum emission peaks, quite the opposite of the situation along the eastern ridge.

We must also consider the kinematics of the region. The multi-channel CI $^3P_1$–$^3P_0$ line map of the central region of S 140 shows there to be both blue and redshifted CI emission produced at the inner edge of the blueshifted molecular outflow cavity wall, as traced by blueshifted $C^{17}O$ emission (Paper II). The situation along the eastern ridge is quite different. Here the CO emission sits inside the CI ridge feature and the observed CI emission is at the velocity of the ambient cloud. The obvious implication is that the CI emission *cannot be produced within the molecular outflow*. Alternatively, the fact that CI emission from eastern ridge is observed at the same velocity as the ambient cloud, and is almost as intense as the CI emission from the PDR at the southwestern edge of S 140, implies it is produced in the same manner.

4.2.2. A self-consistent model for the L 1204/S 140 region

The only morphology for the region that is consistent with all the molecular, atomic and submm continuum data is as follows. The eastern ridge feature is the dense, clumpy edge of the blueshifted outflow lobe that is closest to the observer along the line of sight. This naturally explains the overlapping CS, NH_3, CI and continuum features. The outflow has expanded towards the edge of the

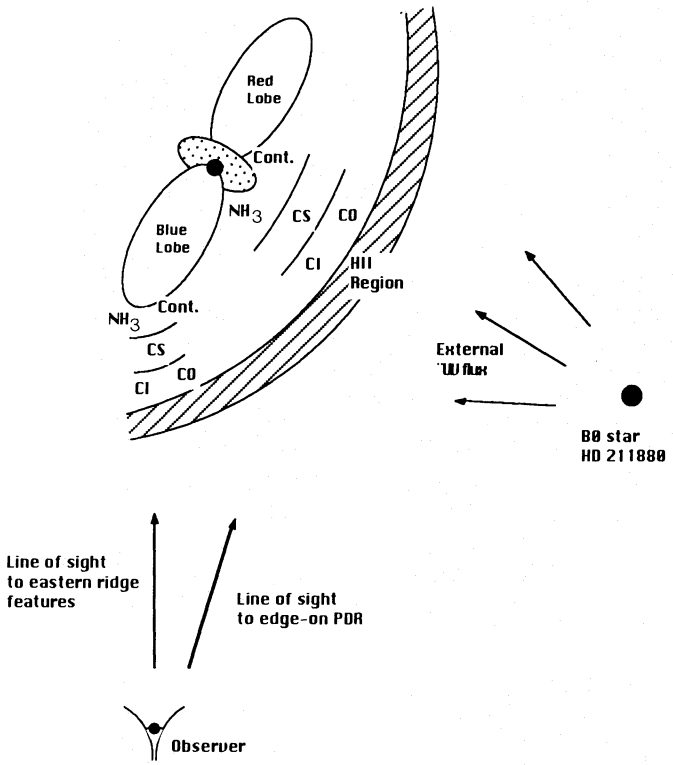

Fig. 4. Schematic representation of the S 140/L 1204 region showing the plane that contains the observer, the external illuminating star HD 211880, the HII region/molecular cloud interface and the embedded molecular outflow. The outflow has expanded towards the edge of the molecular cloud such that the edge of the blueshifted outflow lobe is bounded by the expanding HII region. The outside edge is therefore an externally illuminated PDR. Thus the CI emission emanates from the outer edge of the cloud (the PDR), with the CS emission tracing the compressed high density gas, effectively sandwiched between the expanding outflow and PDR regions. The NH_3 and continuum emission emanates from the inner edge of the outflow lobe, shielded from the external UV field. The CI, CS, NH_3 and continuum emission peaks are along the same observers line of sight and thus appear overlapping. Towards the southwestern rim of the molecular cloud the geometry of the PDR is such that it is edge-on when viewed along the observers line of sight and thus the CI, CS, NH_3 and continuum emission layers are spatially separate and distinct

molecular cloud such that the edge of the blueshifted outflow lobe is bounded by the expanding HII region. The outside edge is therefore an externally illuminated PDR. Thus the CI emission emanates from the outer edge of the cloud (the PDR), with the CS emission tracing the compressed high density gas, effectively sandwiched between the expanding outflow and PDR regions. The NH_3 and continuum emission emanates from the inner edge of the outflow lobe, shielded from the external UV field. A schematic of the region is shown in Fig. 4.

This is also consistent with what we observe from the edge-on PDR at the southwestern rim of the cloud. Here the geometry allows us to observe the different molecular, atomic and continuum emission "layers". The CS, NH_3, CI and continuum peaks are *all* along a line that also connects IRS1 and the external illuminating source. The CI emission peak on the PDR is bounded by the CS peak, with the NH_3 and continuum peaks closest to the centre of the cloud. The close proximity of the CI and CS peaks and the fact that the CS emission along the western ridge is located 10-20 arcsec outside the more centrally peaked continuum emission may imply that, here too, part of the outflow structure is bounded by the expanding HII region, producing a PDR on the outer edge. Velocity channel maps of CS J = 1→0 from Hayashi & Murata (1992), CS J = 3→2 from Stutzki et al. (1994) and NH_3 (1,1) from Zhou et al. (1993), imply that emission along the eastern and western ridges is mainly observed at close to the ambient velocity of the molecular cloud ($\sim$ -8 km s^{-1}), but that many clumps are observed at either blue or redshifted velocities. This is consistent with the scenario of the dense outflow wall compressed from two directions.

4.3. Dust/gas ratio across S 140

Figure 5 shows the 800μm continuum flux density plotted agains $N(C^{18}O)$ values calculated in Paper III. This can be converted to A_v using the relationship of Lada et al. (1994). It should be noted that the Lada et al. relationship was only derived for $A_v \leq 15$, but the results of White & Sandell (1994) suggest it is also accurate for deeper A_v values. The 800μm continuum data was chosen for comparison as the central frequency for this band is close to that for the $C^{18}O$ J=3→2 line, and thus the beamwidths are virtually identical (13–14 arcsec). There is a clear correlation, with the continuum flux density increasing with extinction.

Lines of constant dust/gas mass ratios are shown for an assumed dust temperature of 50K and a grain emissivity of β=1.5. The dust temperature assumed is consistent with that derived in Sect. 4.1 for a 1.5×1.5 arcmin^2 region centred on the position of the infrared cluster (no correction was made for line contamination of the continuum emission, which is only likely to be significant towards the densest parts of the molecular outflow – $\leq$10% – and negligible elsewhere). The data is generally consistent with the canonical dust/gas mass ratio of $\sim$1%. This is particularly true for positions towards the edge-on PDR and lower column density positions towards the outflow ($A_v \leq 70$). For the highest observed column densities (A_v =70–100) the continuum flux density increases rapidly, implying a higher dust/gas mass ratio is appropriate ($\sim$2-5%). Similar observations carried out by White & Sandell (1994) towards the IRC2 and Bright Bar regions of Orion show this increase to continue at even higher densities (their observations cover higher extinctions than found in S 140 – A_v up to $\sim$400), implying an even higher dust/gas mass ratio may be appropriate in these regions, up to 10%.

The higher dust/gas mass ratio observed towards regions of highest column density may be due to 'freeze out' of gas onto the grains (e.g. Mauersberger et al. 1992). In regions of high density ($\geq 10^5$ cm^{-3}) tracer molecules such as CO and isotopes will stick onto ice grain mantles, unless the dust temperature is sufficiently high to allow evaporation.

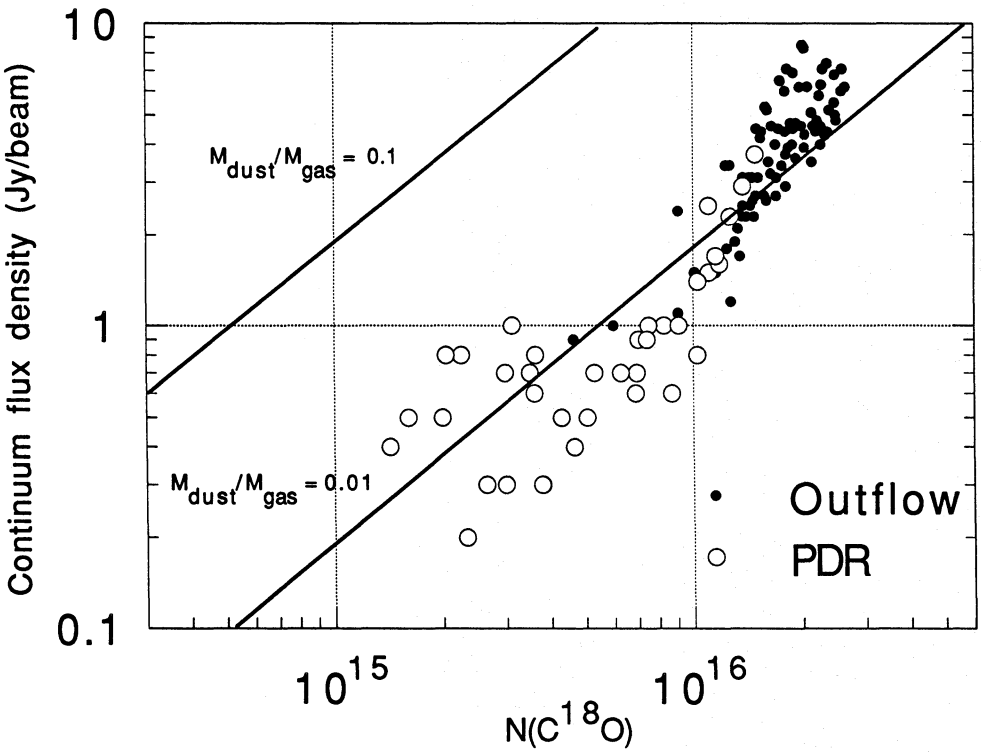

Fig. 5. Graph of the 800μm flux density plotted against $N(C^{18}O)$. Data points are shown for positions towards the bipolar outflow and PDR. Model fits for lines of constant M_{dust}/M_{gas} are shown as bold lines. An assumed dust temperature of 50K and a grain emissivity of β=1.5 are assumed

5. Conclusions

We have mapped the submillimetre continuum emission from the L 1204/S 140 complex in broad bands centred at 450, 800 and 1100μm. The morphology of the region is similar at all three wavelengths, with the emitting region compact, about 90 arcsec in diameter, and centrally peaked around the cloud core. Three new submillimetre sources have been observed which are not coincident with any previously known near or mid infrared sources. It is not possible to determine whether the sources are gravitationally bound, since virial estimates are adversely influenced by the presence of the bipolar outflow. The observation that SMM1 and SMM2 lie either side of the infrared sources, in a line roughly perpendicular to the direction of the bipolar outflow, imply they may be the remnants of a large-scale disk.

Comparison of the continuum emission with previous high resolution CS, NH_3 and CI observations provides evidence that, for the first time, demonstrates the PDR and outflow are intimately linked. The only scenario that is able to explain all of the available molecular and atomic emission line and our submillimetre continuum data is one in which the outflow has expanded towards the edge of the molecular cloud such that the edge of the blueshifted outflow lobe is bounded by the expanding HII region. The CI emission originates from the outer edge of the cloud (the PDR), with the CS emission tracing compressed high density gas, sandwiched between the expanding outflow and PDR regions. The NH_3 and continuum emission emanates from the inner edge of the outflow lobe, shielded from the external UV field.

A plot of the 800μm flux against $N(C^{18}O)$ implies that the dust/gas mass ratio is close to the canonical value ($\sim$1%) at the lower end of the observed extinction range ($A_v \leq 70$), but for the highest observed extinctions (A_v =70–100) the continuum flux density increases rapidly, implying a higher dust/gas mass ratio is appropriate ($\sim$2-5%), possibly indicating freeze-out of gas onto dust grains.

Acknowledgements. We wish to thank Shudong Zhou and Masa Hayashi for supplying greyscale images of their NH_3 and CS data respectively. We also wish to thank Juergen Stutzki for his helpful comments. We acknowledge the PPARC for travel funds, NRM's PDRA and DWT's SRF.

References

André P., Ward-Thompson D., Barsony M., 1993, ApJ 406, 122
Bally J., Lada C., 1983, ApJ 265, 824
Beichman C. A., Becklin E. E., Wynn-Williams C. G., 1979, ApJ 232, L47
Beichman C. A., et al. 1988, IRAS Explanatory Supplement, NASA RP-1190, Washington DC
Blair G. N., Evans N. J., Vanden Bout P. A, Peters W. L., 1978, ApJ 219, 896
Crampton D., Fisher W. A., 1974, Pub. Dom. Ap. Obs. 14, 12
van Dishoeck E. F., Black J. H., 1988, ApJ 334, 771

Duncan W. D., Robson E. I., Ade P. A. R., Griffin M. J., Sandell G., 1990, MNRAS 243, 126
Evans N. J., Kutner M. L., Mundy L. G., 1987, ApJ 323, 145
Evans N. J., Mundy L. G., Kutner M. L., DePoy D. L., 1989, ApJ 346, 212
Griffin M., Orton 1993, Icarus 105, 537
Hackwell J. A., Grasdalen G. L., Gehrz R. D., 1982, ApJ 252, 250
Hayashi M., Murata Y., 1992, PASJ 377, 391
Hildebrand R. H., 1983, QJRAS 24, 267
Hollenbach D. J., Takahashi T., Tielens A. G. G. M., 1991, ApJ 377, 192
Lada C. J., Lada E. A., Clemens D. P., Bally J., 1994, ApJ 429, 694
Lester D. F., Harvey P. M., Joy M., Ellis H. B., 1986, ApJ 309, 80
Mauersberger R., Wilson T. L., Mezger P. G., Gaume R., Johnson K. J., 1992, A&A 256, 640
Minchin N. R., White G. J., Padman R., 1993, A&A 277, 595 (Paper I)
Minchin N. R., White G. J., Stutzki J., Krause D., 1994, A&A 291, 250 (Paper II)
Minchin N. R., White G. J., Ward-Thompson D., 1994, A&A submitted (Paper III)
Orton G. S., Griffin M. J., Ade P. A. R., Nolt I. G., Radostitz J., Robson E. I., Gear W. K., 1986, Icarus 67, 289
Rengarajan T. N., 1984, A&A 140, 213
Richer J. S., Padman R., Ward-Thompson D., Hills R. E., Harris A. I., 1993, MNRAS 262, 839
Sandell G., 1994, ApJ, in press
Snell R. L., Scoville N. Z., Sanders D. B., Erickson N. R., 1984, ApJ 284, 176
Stutzki J., Stacey G. J., Genzel R., Harris A. I., Jaffe D. T., Lugten J. B., 1988, ApJ 332, 379
Stutzki J., Krause D., Johnen C., Minchin N. R., Gusten R., 1994, A&A submitted
Tielens A. G. G. M., Hollenbach D. J., 1985, ApJ 291, 722
White G. J., Padman R., 1991, Nature 354, 511
White G. J., Sandell G., 1994, A&A in press
Zhou S., Evans N. J., Mundy L. G., Kutner M. L., 1993, ApJ 417, 613

This article was processed by the author using Springer-Verlag LaTeX A&A style file version 3.